Realistic Leading-Edge Roughness Effects on Airfoil Performance

Robert S. Ehrmann[*] and Edward B. White [†]

Texas A&M University, College Station, TX 77843-3141

Mark Rumsey[‡]

Sandia National Laboratories, Albuquerque, NM 87185

Raymond Chow[§], Christopher M. Langel[¶], and C.P. van Dam[‖]

University of California, Davis, Davis, CA 95616

Wind farm operators have observed production decay over time, with the exact cause unknown and difficult to quantify. A common explanation is blade surface roughness, as wind turbines are continuously subjected to environmental hazards. Difficulty arises in understanding and quantifying performance degradation. Historically, wind turbine airfoil families were designed to be insensitive to roughness by simulating roughness with 2D trip strips. Despite this, roughness is still shown to negatively affect airfoil performance. Experiments have also illustrated that random-distributed roughness is not properly simulated by trip strips. Therefore, to better understand how real roughness affects performance, field measurements of turbine-blade roughness are made and simulated on an airfoil section in a wind tunnel. This data will serve to validate and calibrate a one equation roughness amplification model that interacts with the Langrty-Menter transition model. The observed roughness contained 2D steps, heavy 2D erosion, pitting, insects, and repairs. Of these observations, 2D steps from paint chips are characterized and recreated for this particular wind tunnel entry. The model is tested at chord Reynolds numbers up to 3.6×10^6. Measurements of lift, drag, and pitching moment are made with and without roughness contamination. Transition location is acquired with infrared thermography and a hotfilm array. Numerical simulations are only compared to the clean configuration and match well to lift, drag, and transition for $Re_c = 1.6 \times 10^6$. However, drag is overpredicted at $Re_c = 3.2 \times 10^6$. The paint roughness observes a consistent increase in drag compared to the clean configuration.

I. Introduction

Wind farms are plagued with initial underperformance compared to manufacturer predictions and performance deterioration over time. Capacity factors have been overestimated by 10% to 15%.[1] Some manufacturers offer production guarantees; if turbines fail to reach a promised capacity factor, the manufacturer will pay the difference. As these are dollars lost, research is underway to pinpoint these losses. One possible aerodynamic explanation is blade roughness caused by erosion (sand, salt, and hail), foreign deposits (insects), and coating spallation, which decrease performance by decreasing the section maximum lift and increasing drag.[2] Erosion has been observed to result in 20% or greater loss in energy capture and can affect blades that have been operating for as little as three years.[3,4] Blade erosion has become a significant enough problem that 6% of all wind turbine related repairs are due to blade damage.[5]

---

[*]Graduate Research Assistant, AIAA Student Member.
[†]Associate Professor, Associate Fellow AIAA.
[‡]Senior Member of Technical Staff.
[§]Postdoctoral Scholar.
[¶]Graduate Student Researcher.
[‖]Professor & Chair, Associate Fellow AIAA.

American Institute of Aeronautics and Astronautics

Roughness is currently characterized as 2D (trip strips or steps), isolated or arrayed 3D, or distributed 3D. The transition phenomena is characterized differently for each roughness type. Boundary layers with 2D roughness illustrate forward-moving transition as Re_k increases to $Re_{k,\text{crit}}$.[6] Isolated 3D roughness has been found being more critical than 2D roughness.[7] If $Re_{k,\text{crit}}$ is exceeded, transient growth briefly occurs, followed closely by bypass transition, but the transition front shows little movement for subcritical Re_k. Typical critical roughness Reynolds number values for height to diameter ratios near unity range from 600 to 900.[8]

Downs et al. tested patches of distributed roughness on a flat plate.[9] For supercritical roughness, the transition mechanism was similar to that of isolated 3D roughness. Neither TS-like profiles nor TS-band disturbance frequencies were observed. This suggests transition for supercritical roughness occurs by the bypass mechanism. The measurement domain was insufficient to show transition for the subcritical case. If subcritical, the steady transient disturbances would hasten the onset of transition, similar to Ergin and White.[10]

White et al. tested a NACA $63_3 - 418$ with a clean, tripped, low-k, and high-k leading edge.[2] The low-k leading edge was sandblasted aluminum while the high-k leading edge was rapid-prototyped random distributed roughness. The low-k and high-k leading edge roughness was generated in Fourier space with randomly selected amplitude and phase coefficients.[9] The longest chordwise and spanwise wavelengths were 50 mm while the shortest wavelength were 2 mm. The roughness height was scaled such that the maximum height was 1.2 mm. The sand blasted leading edge had a maximum height of 70μm. As expected, the increased roughness decreased $c_{l,\text{max}}$ and increased c_{d0}. The tripped leading edge had a slightly higher $c_{l,\text{max}}$ and generally lower c_d than the low-k. A significant result was that the trip tape proved to be unrepresentative of roughness.

The NREL and Risø wind turbine airfoil series were numerically designed in the nineties with the goal that the maximum lift coefficient was insensitive to roughness.[11,12] It was found that sensitivity to roughness was higher than expected in the Risø-A1 series.[12] New profiles, Risø-B1 series, were designed and validated with representative roughness created with a trip strip.

While the data from White et al. raises concern over the validity of the NREL and Risø airfoil's insensitivity to roughness, realistic wind turbine roughness has yet to be tested. Therefore, a need exists to accurately model wind turbine roughness and rough wind turbine blade performance, thereby allowing high-fidelity CFD codes to be validated. Once validated, CFD can be utilized to design blades with lower sensitivities to roughness.

A significant survey of in-service turbomachinery turbine blades was made by Bons.[13] While wind and gas turbines are inherently different in scale and angular velocity, many similar characteristic features were observed: deposits, erosion, pitting, and coating erosion. Bons notes that most turbine roughness studies have utilized uniform sand-roughened walls, which are unrepresentative of real roughness.[14] Reuss et al. simulated insect roughness on various wind turbine blades with individual particles of grit.[15] The insect pattern was designed from measurements on an in-service turbine, but few details are reported. To the author's knowledge, no detailed, open-literature exists surveying wind turbine blade roughness.

This issue is being investigated through a collaboration between Sandia National Laboratories, U.C. Davis, Texas A&M, and industry partners. The research has undergone several stages, including the collection of field measurements of erosion profiles and performance degradation, the wind tunnel testing of an airfoil with a range of erosion profiles, and the development of a computational fluid dynamics (CFD) model. This combined effort is driving towards a detailed understanding of the effects of erosion phenomenon, as well as an engineering-level model that can be used to influence airfoil blade design, optimum maintenance scheduling, wind farm siting, and project financial planning.

This current work focuses on describing observed roughness, reporting experimental capabilities, introducing simulation methodology, and comparing preliminary experimental and computational results. Experimental testing will yield aerodynamic performance data on highly eroded, 2D blades with roughness characteristic of measured, in-service blades. Testing will also elucidate the relevant transition phenomena. To accomplish this, the real blade roughness is measured and parameterized. The roughness is simulated on a representative blade-airfoil section, reproducing in-service conditions and allowing for comparisons against a clean configuration. This data is utilized to calibrate a one equation roughness amplification model that interacts with the Langtry-Menter transition model. With the model tuned, wind turbine performance can be better predicted and future airfoil series created to have lower roughness sensitivity.

American Institute of Aeronautics and Astronautics

II.   Roughness Characterization

The parameterization of roughness has been one of the many hurdles encountered in previous investigations. Roughness is often considered as random or uniform, ignoring chord or span variation or characteristic lengths. To improve this, in-service wind turbine blades are measured with castings and a laser scanner. The roughness is characterized into general types which are simulated on a wind tunnel model.

Roughness on blades of three, in-service wind turbines, each having three blades, is cataloged. General modes of erosion have been defined with pictures. Laser scans and castings at these locations were then made. Large-scale roughness is measured with the Creaform EXAscan, a portable laser scanner with 0.2 mm resolution. Small-scale roughness is recorded with castings. Impressions of the roughness are made with dental alginate which is spatially unstable over long periods of time. Therefore, lab stone castings of the dental alginate are made within 24 hours of the original casting. At a later time, the lab stone castings are measured with a Keyence LK-H022 laser displacement sensor. The laser has a 25μm spot diameter with 0.02μm vertical repeatability.

Observed roughness types are organized into 2D heavy erosion, 2D inboard steps, random pits, repairs, insects, and 2D paint. Only the 2D inboard steps and insect roughness are repeatable between turbine blades. The heaviest erosion occurs near the blade tip at the highest local blade velocities. Otherwise, there is large variation between occurrence and location of the roughness, despite similar operating conditions.

Of the nine observed blades, the most significant damage is the 2D heavy erosion. It is characterized by locations of erosion penetrating the paint and gelcoat, exposing the blade fiberglass. This erosion is found on the outboard two meters of the blade. The 2D inboard step begins near the turbine hub and continues outboard to 75% span. In some locations, the step is better described as an indentation. There is chordwise variation in the step location. Some span locations have multiple steps at different chord locations. A possible explanation of the step occurrence is bond-line joint exposure. Random pits occur on all of the blades in varying amounts. The pitting penetrates the paint and gelcoat exposing the fiberglass, similar to the 2D erosion, but are still unique in having an aspect ratio of nearly one. Pits are thought to precede 2D erosion. One blade has undergone repairs to the leading edge. Leading edge protection (LEP) is applied over the repaired sections. Over time, the LEP material eroded, yielding spanwise ridges. The edges of the LEP result in a backwards facing step on both the suction and pressure sides.

Insect roughness is characteristically different from erosion since it is a foreign deposit, adding to the airfoil outer mold line. Insects generally impact the blade within the first 10% of the chord. The insect bodies remain more intact near the leading edge. Further aft, the insect smears, resulting in chordwise streaks. There is likely spanwise variation in the insect roughness, but it was not easily measurable. Preliminary profilometer scans indicate the insect roughness to be minimal. Additional image investigation indicated the blades, while dirty, generally had low roughness. A possible explanation of minimal insect roughness is the 5.4 inches of rain received one month prior to measurement.

Lastly, the 2D paint erosion is characterized as paint which has eroded or chipped off the leading edge of the blade. This yields a forward-facing step on both the suction and pressure sides of the blade. The spanwise and chordwise locations of the 2D paint step are inconsistent. Scans from the laser profilometer indicate an average step height of 150μm, varying by $\pm25\mu$m depending on span location. The span variation is minimal and ignored. The paint is assumed to chip off in constant thicknesses. Because of this, paint roughness near the leading edge will likely transition the flow while roughness further aft may or may not transition. Hence, the further aft roughness is of greater interest.

Assuming a linear velocity gradient near the wall, the velocity at a given height, $u(k)$, may be written as

$$u(k) = \frac{k\tau_w}{\mu} \tag{1}$$

where k is the roughness height, τ_w is the wall shear stress, and μ is the dynamic viscosity. The Reynolds number based on roughness height, Re_k, is then defined as

$$Re_k = \frac{k^2\rho\tau_w}{\mu^2} \tag{2}$$

Figure 1a illustrates an example of aft 2D paint roughness at 10% chord on average. The local step height of the paint is $142 \pm 16\mu$m. Assuming general operating conditions, the local chord Reynolds number is $Re_c = 5.2 \times 10^6$. XFOIL is used to estimate the local wall shear stress at the 10% chord location. Using

Eq. 2, the 2D paint roughness has an $Re_k = 186$. To yield experimental Re_k both higher and lower than the measured value, the roughness is designed to match $Re_k = 186$ at a model $Re_c = 2.4 \times 10^6$, yielding a nominal roughness height of $134\mu m$. The paint roughness is simulated by laying contact paper from 10% to 60% chord on the suction side of the model. The contact paper is measured to be $157 \pm 6\mu m$, 17% thicker than the nominal step height. This yields actual Re_k of 46 ± 4, 130 ± 10, 238 ± 19, 366 ± 29, and 437 ± 34 for tested Re_c of 0.8, 1.6, 2.4, 3.2, and 4.0×10^6, assuming $\alpha = 4.75°$.

The leading edge of the contact paper has a profile cut into it, shown in Fig. 1b, simulating the profile of the observed paint roughness chips. Since the boundary layer is thinner on the operational wind turbine than in the designed test, the roughness profile must also be scaled. The roughness is scaled by the local displacement thickness for the operational wind turbine at $Re_c = 5.2 \times 10^6$ to the wind tunnel model at $Re_c = 4.0 \times 10^6$, scaling the paint roughness by 1.15.
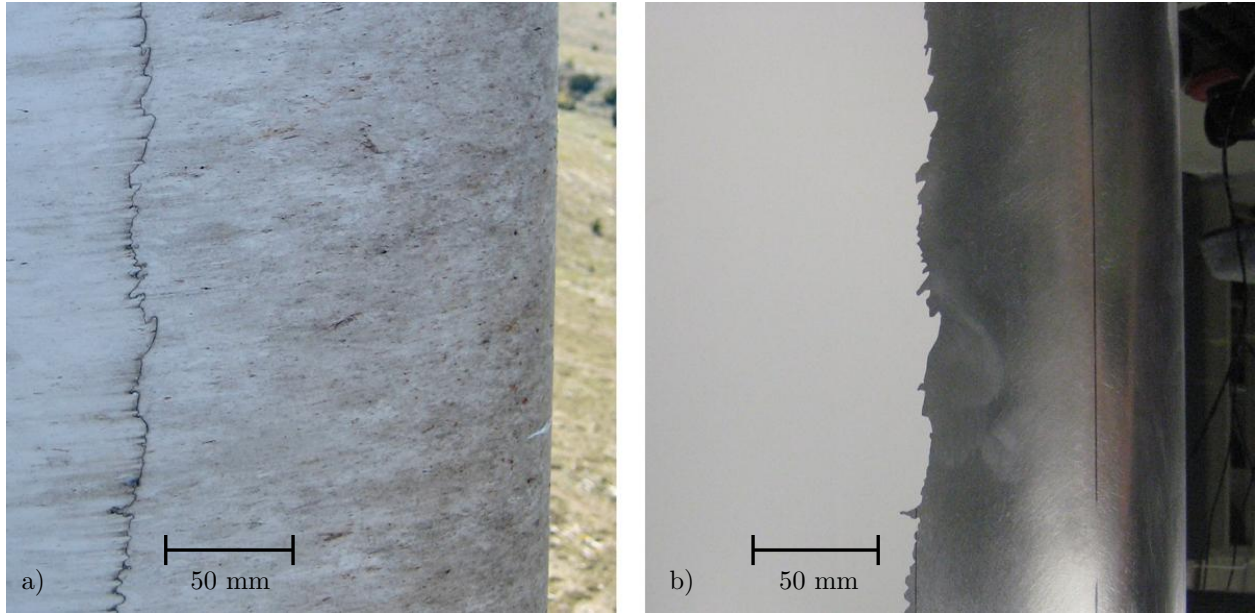
Figure 1: Image of 2D paint roughness a) observed in-service and b) simulated on wind tunnel model.

III.   Experimental Approach

The model is tested at the Texas A&M Oran W. Nicks Low Speed Wind Tunnel (LSWT). The LSWT is a closed-return tunnel with a 7 ft×10 ft test section and can achieve freestream velocities of 75 m/s. For the given test conditions, the wind tunnel has a turbulence intensity of 0.25% and flow uniformity within the Pitot-static measurement uncertainty.[16] The wind tunnel has an external floor balance to which the wing is mounted.

The wind tunnel model is a NACA $63_3 - 418$. As CFD validation is the preliminary purpose of the testing, a nonproprietary airfoil is chosen, opening potential future validation efforts. The trailing edge is 1.9 mm thick for manufacturability. In order to achieve the unique erosion configurations, the model is designed to be modular with a removable leading edge at 15% chord. Prior testing by White et al. found lift and transition to be highly sensitive to gaps in the model, caused by an insufficient stiff structure.[2] Ideally, the model would be sufficiently stiff, removing gap issues, while being easily installed. To achieve this, the model is manufactured from aluminum and designed for minimal deflections. Two piano hinges along the upper and lower mainbody are used to securely attach the leading edge. The hinge pins can be removed through holes in the wind tunnel wall, allowing simple model changes while creating a stiff interface between the leading edge and airfoil main body.

The model mounts vertically, attaching to the wind tunnel floor balance and to a compliant system mounted above the ceiling. Pitch variation is achieved with by rotating the floor balance. Before mounting to the ceiling, the model is centered and made perpendicular to the floor balance rotation plane, ensuring

little motion near the ceiling. Since floor balance does not have a true center of rotation, there will always be eccentricity in the model motion. If the model is simply cantilevered to the floor balance, it would quickly overload the balance. It is therefore also attached to the ceiling. However, if the ceiling mount is stiff, the eccentricity in the floor balance rotation will overload the floor balance in the wind-off condition.

To remedy this, a compliant ceiling mount is designed. A spherical bearing is held in place with six pneumatic cylinders. The spherical bearing allows the model to freely rotate. As it rotates, the pneumatic cylinders allow deflections for small eccentricity and misalignments in the floor balance. However, at higher loadings, the cylinders also provide the necessary stiffness to maintain deflections less than 15 mm.

The airfoil is tested in three configurations: clean, trip strip, and paint roughness. The clean configuration has a piece of Scotch®tape applied over the leading edge seam at 15%. Further discussion of this is found below. The trip strip is placed at 2% and 5% chord on the upper and lower surfaces, respectively. This forces transition and yields effectively completely turbulent flow. The trip strip is $459 \pm 2 \mu$m thick with a $60°$ zigzag pattern that has a 7 mm amplitude. Paint roughness is simulated by placing contact paper over the upper surface of the model. Contact paper is not applied on the lower surface since transition in a favorable pressure gradient is greatly delayed and less critical to airfoil performance. Further description of the paint roughness is found in Section II.

Numerous measurements are completed on the model, including lift, drag, moment, boundary layer profiles, transition location, and skin friction. Lift and moment are measured by integrating surface static pressure measurements. Drag measurements are completed by measuring the velocity deficit with a wake rake and applying a control volume approach. A boundary layer rake is placed at 50% chord and 22% span to yield boundary layer profile information. Pressure measurements are made with three ESP-HD pressure scanning units with accuracies of ± 5 Pa and ± 10 Pa.

Transition is measured with two techniques. First, infrared (IR) thermography is applied.[17] IR thermography leverages the difference in convection rates of laminar and turbulent flows to indicate transition location. Generally, the surface temperature lapses the ambient temperature due to viscous and motor heating. The warmer, ambient air will heat a turbulent region faster than a laminar region. Utlizing an IR camera, this will indicate transition location on the model. If the model and tunnel temperature are similar, an internal heating sheet can heat the model above ambient temperature. In this case, the cooler ambient air will cool turbulent regions faster than laminar ones. IR cameras are unable to view through glass, requiring a hole in the tunnel wall. Due to a small variation in tunnel static pressure to atmospheric pressure, a pressue box is built around the camera.

The second method is hotfilm anemometry. A Senflex®93021 hotfilm from Tao of Systems Integration, Inc. is applied to the model. The hotfilm has 28 sensors which are all placed at 38% span. The first sensor is at 20% chord with the last at 41% chord. An image of the hotfilm is shown in Fig. 2 with the aluminum leading edge shown at right. The sensors are attached to two seperate anemometers: a constant temperature anemometer (CTA) and constant voltage anemometer (CVA). The CTA circuit has low thermal inertia yielding an excellent time response. The CVA circuit used is essentially steady state. However, the CVA can be calibrated *in situ* against a Preston tube, resulting in skin friction measurements. Hotfilm sensors 1, 5, 12, 16, 20, and 28 are attached to an A.A. Lab Systems AN-1003 CTA system while sensors 2, 6, 9, 13, 17, 21, and 27 are attached to an in-house CVA. The CTA is bandpass filtered with a Kemo VBF44 between 1 Hz and 10 kHz. The signal is sampled at 75 kHz.

Drag is found to vary depending on wake position. Generally, the flow behind the pressure ports is turbulent, leading to increased drag. Therefore, the wake rake is placed 0.4572 meters above the model centerline, resulting in a more proper drag measurement. Future testing will determine drag sensitivity to wake position. Drag is reduced when a piece of Scotch®tape is applied over the leading edge gap. The leading edge gap is $590 \pm 75 \mu$m wide. The depth is not measurable due to stylus interference. When covered with tape, shown in Fig. 3 the gap depth is approximately equal to the tape thickness. At the maximum chord Reynolds number of 3.6×10^6, the Scotch®tape has an $Re_k = 45 \pm 5$. Smith determined that a 2D step approximately has no influence when $Re_k < 50$.[18]

Additional testing suggested that air was flowing from the gap at higher angles of attack, creating a small jet at the leading edge. The physical gap between between the leading edge and airfoil main body may also have caused the drag rise. The precise mechanism resulting in drag improvement from the tape is not known. Future testing will investigate spanwise variation in drag.
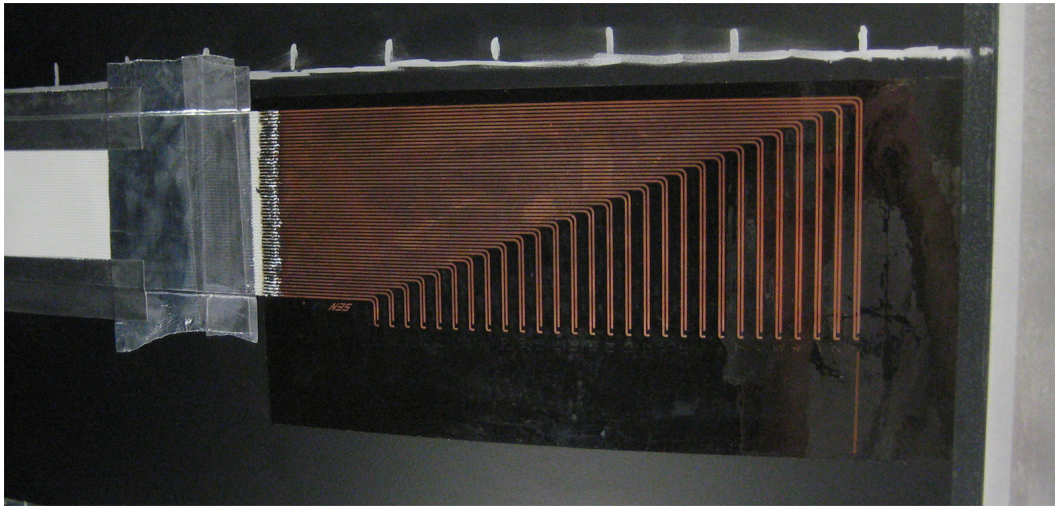
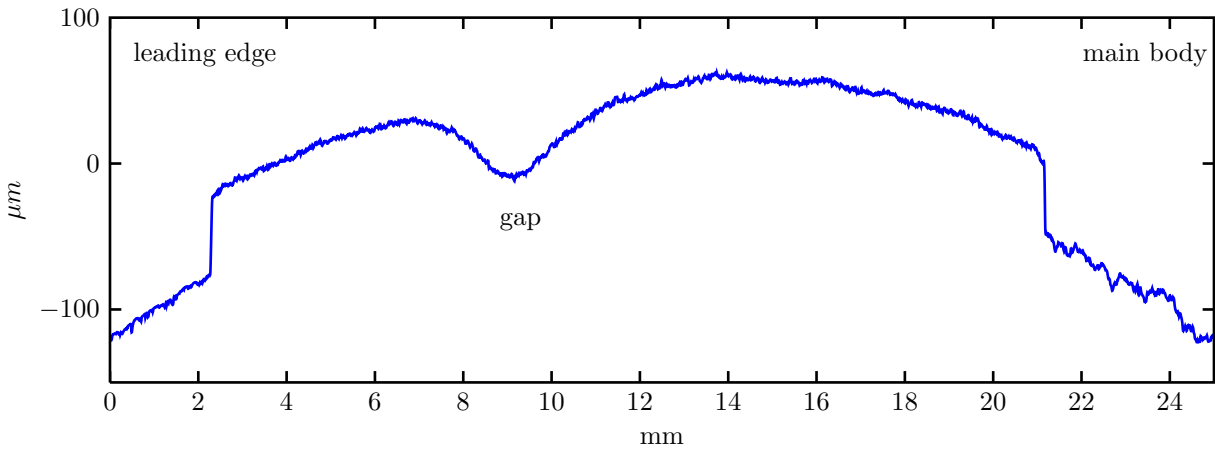Figure 2: Image of the installed hotfilm.

Figure 3: Profile of Scotch®tape over the leading edge gap.

IV.   Experimental Methodology

Lift is measured by integrating the surface pressure distribution. Since there is no static pressure measured at the trailing edge, a weighted average is estimated from the nearest two ports. The wind tunnel vents to atmospheric pressure. However, there is a slight variation between measured tunnel static and atmospheric pressure. This difference results in a non-unity stagnation pressure coefficient. To remedy this, the difference between the maximum pressure coefficient and one is applied to the distribution, correcting for the static pressure offset. The normal coefficient, c_n is then defined as

$$c_n = -\int C_P d(x/c) \tag{3}$$

where $C_P = \Delta p/q_\infty$. The lift coefficient, neglecting the axial coefficient, is then approximately $c_l = c_n \cos\alpha$. Moment coefficient, c_m, is calculated in a similar manner where

$$c_m = \int C_P(x/c)d(x/c) \tag{4}$$

where the pressure coefficient is multiplied by a moment arm, x/c, yielding the final moment. Drag is calculated using the momentum deficit technique and is determined by

$$c_d = 2 \int \left(\sqrt{\frac{q}{q_0}} - \frac{q}{q_0} \right) d(y/c) \tag{5}$$

where q is the dynamic pressure, q_0 is the upstream dynamic pressure, and y/c is the nondimensional direction normal to both chord and span. Due to circulation, q_0 is determined from the local dynamic pressure just outside of the wake measurement, yielding a deficit shown in Fig. 4. It is noted that near stall, the wake is unsteady and unrepeatable, shown in Fig. 5.
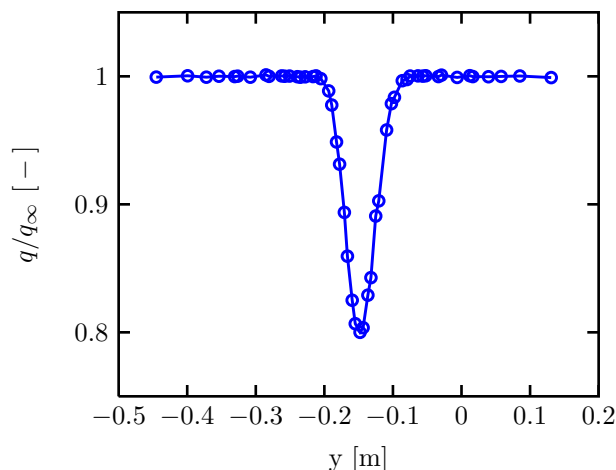
Figure 4: Velocity deficit at $\alpha = 8°$.
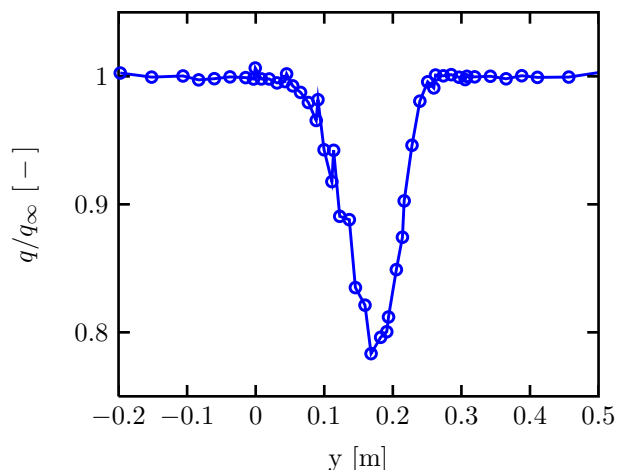
Figure 5: Velocity deficit at $\alpha = -14°$.

Boundary corrections are made as specified in Barlow et al.[19] In brief, corrections are made to velocity terms accounting for solid and wake blockage. Additional correction is added for streamline curvature, correcting angle of attack, lift, drag, and moment. Because no direct drag measurements are made beyond stall, drag is estimated using data from Sheldahl and Klimas.[20]

To determine transition locations, IR images are acquired at various angles of attack. Variations in surface temperature are used to indicate transition location, as seen in Fig. 6. Ticks at 5% chord intervals on the model surface are used to determine transition location. Currently, images are analyzed by sight which is sufficiently accurate (± 1% chord) for a 2D transition front. A transition location for turbulent wedges proves more difficult to define (± 10% chord) and requires computational analysis.
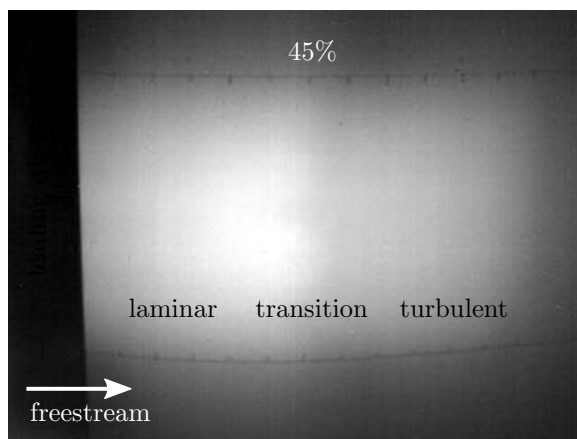

Figure 6: IR image of transition at $Re_c = 2.4 \times 10^6$ and $\alpha = 2°$, indicating transition at 45% chord.

Analysis of the CTA channels follows the recommendations of Press et al.[21] Each data sequence is broken

into 15, 50%-overlapped blocks. A Welch window is applied to each block and a single power spectrum is estimated from the average of the Fourier coefficients.

The CVA output is utilized to measure skin friction, but must be calibrated *in situ* against a measured skin friction at multiple Reynolds numbers. Calibration is achieved with a Preston tube at low Reynolds numbers and XFOIL at higher Reynolds numbers since the boundary layer is too thin to yield proper Preston tube data. The CVA output, Φ, is recorded for each channel. The measured shear stress is fit to

$$\Phi = A\tau^{1/n} + B \tag{6}$$

where A, B, and n are calibration coefficients.

V. Computational Methods for Transition Prediction

A common engineering approach to analyzing complex flow problems is the use of Reynolds-averaged Navier-Stokes (RANS) simulations. Fundamentally RANS procedures require the use of a complementary closure or turbulence model to fully represent practical flows. Unfortunately these models fail to account for many physical mechanisms that cause a boundary layer over a solid to transition from laminar to turbulent. This is not easily corrected as many factors can ultimately cause the breakdown of a laminar boundary layer into a characteristic turbulent form.

Historically several methods have been used to quantify the criteria necessary for a boundary layer to begin transition. Stability based techniques such as the e^N method of van Ingen have proven to accurately represent natural transition, however implementation into RANS codes requires extremely fine near wall grid resolution and the computation of integral values, restricting use in general purpose CFD codes.[22] A recently developed alternative approach is that of local correlation-based transition modeling (LCTM).[23] The general concept is to introduce an empirically correlated quantity based on freestream values that is subsequently compared to local flow conditions and used to indicate when the flow begins to transition. The appeal is that LCTMs are designed to predict boundary layer transition entirely based on local flow quantities allowing parallelization and use on unstructured grids.

A. Langtry-Menter Model

The primary local correlation-based transition model is referred to as the Langtry-Menter, $\gamma - \tilde{R}e_{\theta t}$ model, it introduces two non-physical flow parameters that work in conjunction with one another to determine the criteria the local flow has to meet to induce transition, and once triggered, ramp up to the fully turbulent model.[24][25][23]

The first of the two variables the Langtry-Menter transition model relies on is "intermittency" (γ). It differs from the physically defined parameter of the same name in that it does not represent the exact turbulent state of the boundary layer but acts as a scaling parameter. Within a laminar boundary layer the intermittency variable shuts off the production of turbulent kinetic energy (k), and once local criteria are met, it is used to progressively activate k production.

The second variable is defined as the "Transition Onset Momentum Thickness Reynolds Number" ($\tilde{R}e_{\theta t}$). It is designed to take an empirical correlation based on freestream turbulence intensity and local pressure gradient and introduce local effects using a transport equation. The quantity $\tilde{R}e_{\theta t}$ is compared to other local flow quantities and used to trigger intermittency production and subsequent ramping of turbulent kinetic energy, attempting to mimic the physical transition process. Two transport equations are used to define the distribution of γ and $\tilde{R}e_{\theta t}$ and are defined,

$$\frac{\partial(\rho\gamma)}{\partial t} + \frac{\partial(\rho U_j \gamma)}{\partial x_j} = P_\gamma - E_\gamma + \frac{\partial}{\partial x_j}\left[\left(\mu + \frac{\mu_t}{\sigma_f}\right)\frac{\partial\gamma}{\partial x_j}\right] \tag{7}$$

$$\frac{\partial(\rho\tilde{R}e_{\theta t})}{\partial t} + \frac{\partial(\rho U_j \tilde{R}e_{\theta t})}{\partial x_j} = P_{\theta t} + \frac{\partial}{\partial x_j}\left[\sigma_{\theta t}\left(\mu + \mu_t\right)\frac{\partial\tilde{R}e_{\theta t}}{\partial x_j}\right] \tag{8}$$

The production term within the intermittency equation (P_γ) is a strong function of $\tilde{R}e_{\theta t}$. Also included is an explicit destruction term (E_γ) to account for the possibility of relaminarization. The term $P_{\theta t}$ is used to modify the freestream empirical correlation according to local flow conditions. A more detailed description and full equation set can be found in Langtry and Menter.[25]

B.   Surface Roughness Considerations

Despite the Langtry-Menter model accounting for many different modes of transition, it lacks the ability to simulate the effects of surface roughness. In an attempt to include the influence of surface roughness on boundary layer transition, Dassler, Kozulovic, and Fiala introduced a third term to the Langtry-Menter model; the "Roughness Amplification" (A_r) variable, and it is treated as an additional non-physical quantity that will be produced at rough surface boundaries.[26]   Using a scalar transport equation the variable is convected into the flow field and defines a region of roughness influence to locally modify the transition model downstream of a rough section. The variable attempts to represent the build up of roughness induced perturbations and modify the criteria for transition onset accordingly. The form of the equation allows these time histories of increased turbulent kinetic energy production to be convected away from the roughness itself and promotes an experimentally observed lag between encountering the rough section and the effects seen on boundary layer flow.[27] The equation takes a similar form to those of the transition model;

$$\frac{\partial(\rho A_r)}{\partial t} + \frac{\partial(\rho U_j A_r)}{\partial x_j} = \frac{\partial}{\partial x_j}\left[\sigma_{ar}\left(\mu + \mu_t\right)\frac{\partial A_r}{\partial x_j}\right] \tag{9}$$

The A_r transport equation does not include an explicit production term, alternatively the distribution of A_r is determined with a boundary condition at rough walls where the user inputs a representative equivalent sand grain roughness height (k_s). In general its interaction with the transition model is to drive down the local $\tilde{R}e_{\theta t}$ downstream of rough sections, where high levels of A_r occur. This is accomplished by modifying the production term for $\tilde{R}e_{\theta t}$ to decrease as a function of A_r. In lowering $\tilde{R}e_{\theta t}$, the value the local strain rate must obtain to trigger intermittency production will ultimately be decreased, and therefore the onset of transition will occur with smaller flow disturbances.

VI.   Roughness Model Implementation

A.   OVERFLOW

OVERFLOW is a structured overset, Reynolds-averaged Navier Stokes flow solver.[28] As a flow solver, it is very robust and comprehensive, allowing for the selection from a variety of numerical schemes, turbulence models, boundary conditions, and time advancement schemes.[29] For this study the aforementioned roughness amplification model has been implemented in OVERFLOW.

For all cases the primary flow variables are calculated with sixth-order central differencing using the approximate-factorized form of the Beam-Warming pentadiagonal scheme.[29] The spatial fluxes of the roughness model are discretized using a modified Harten-Lax-van Leer (HLLC) upwind scheme as extension of the existing Langtry-Menter model with the linear matrix solved using a similar successive symmetric over relaxation (SSOR) algorithm.

B.   Flat Plate Distributed Roughness

To provide a baseline for the effects of distributed surface roughness, the model has been re-calibrated on several flat plate test cases in comparison with the experimental results of Feindt and the original CFD model results of Dassler et al.[30,26]

The effect on skin friction of varying non-dimensional sand grain roughness heights with zero pressure gradient test cases are shown in Fig. 7 with transition onset defined as the chordwise location that the minimum skin friction value occurs.

C.   NACA 0012 with Leading Edge Roughness

The results from the flat plate test cases show good agreement with experimental results however more complex geometries are necessary to evaluate the validity of the model. The experimental results of Kerho and Bragg were used to asses the behavior of the model applied to an airfoil with varying roughness locations and extents.[31,32] All tests were performed on a NACA 0012 airfoil of chord length 0.5334 m using a tape strip with hemispherical shapes simulating distributed roughness. The roughness strips were nominally 0.35 mm high including the tape substrate and the center to center spacing of the rough elements was 1.3 mm. The authors report the location of the start of the roughness measured in mm from the leading edge center and
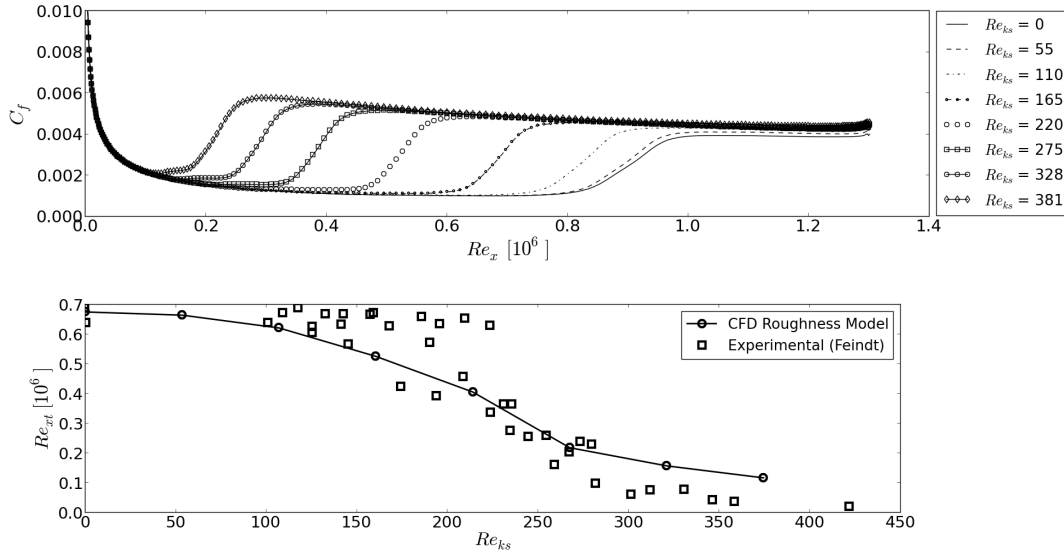
American Institute of Aeronautics and Astronautics

Figure 7: (Top) Skin friction (C_f) for various non-dimensional sand grain roughness heights. (Bottom) Re_{ks} plotted against transition location (Re_{xt}) compared to the experimental results of Feindt.[30] Flat plate with zero pressure gradient, $\alpha = 0°$, Mach $= 0.1$

chordwise length of the rough region in inches. This labeling convention is used in this study to provide a means of referencing particular test configurations.

The results from the experiment indicate a dependence on the location of the surface roughness and demonstrate the desired lag effect between encountering roughness and the appearance of a turbulent boundary layer.
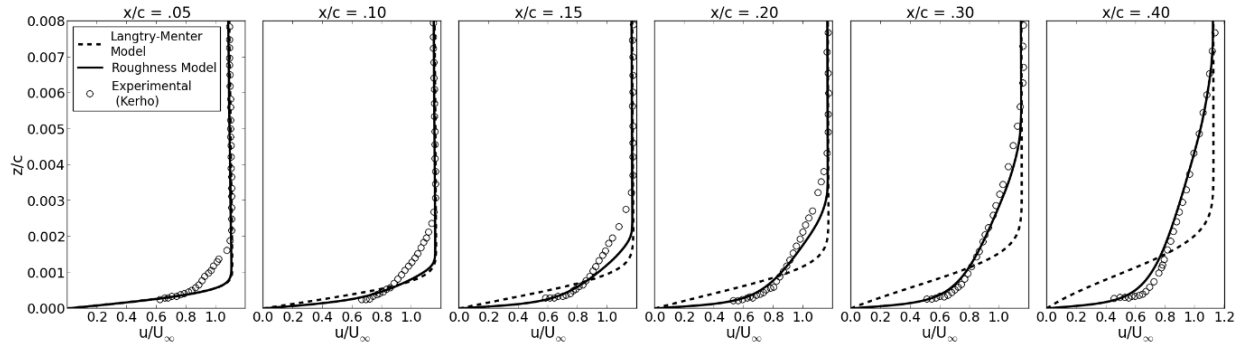
Figure 8: Boundary layer profiles: Kerho [8], unmodified Langtry-Menter transition model, computational roughness model. NACA 0012 airfoil, $Re = 1.25 \times 10^6$, $\alpha = 0^o$, $Tu = 0.1\%$, distributed roughness applied $x/c = 0.0018 - 0.0191$

There is a slight delay in the computational predicted boundary layer profile compared to that of the experiment, this can be attributed to a number of reasons. Primarily intermittency ramping is limited within the transition model, and furthermore the turbulence model itself requires some downstream build up before the full appearance of turbulent kinetic energy.

The computational model accurately reacts to changes in the placement of the rough section and although onset is delayed it tracks the change in transition location well between different rough configurations. The onset of transition is defined for the experimental tests by Kerho as the location the integrated intermittency profile begins to spike. Due to the nature of RANS simulations this parameter cannot be represented computationally, so the boundary layer shape factor ($H = \delta^*/\theta$) was used as indicator for the onset of
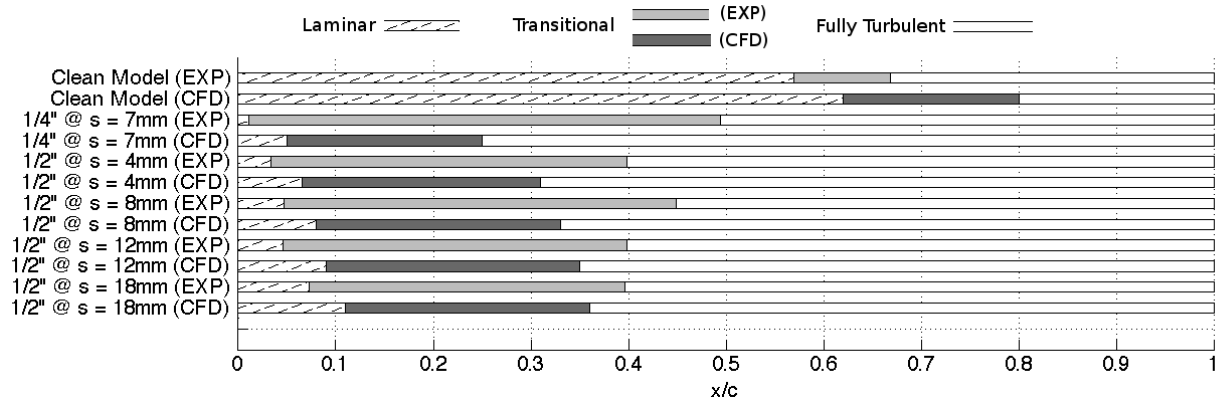
American Institute of Aeronautics and Astronautics

Figure 9: Comparison of boundary layer states with experimental results of Kerho and Bragg [8, 9] for upper surface of NACA 0012 in clean and rough configurations, $Re = 1.25 \times 10^6$, $\alpha = 0^o$, in all test cases.

transition. Typically there will be a rise in the shape factor as the laminar boundary layer grows followed by an inflection when transition begins. The criterion for fully a fully turbulent boundary layer was the chord wise location the boundary layer obtained self similarity when normalized by momentum thickness (θ) as used by Kerho.

VII. Results

The wind tunnel model is tested in three configurations: clean, trip strip, and paint roughness. The configurations are tested at chord Reynolds numbers of 0.8, 1.6, 2.4, 3.2, and 3.6 million. For a general comparison to preliminary CFD results, the $Re_c = 1.6 \times 10^6$ and $Re_c = 3.2 \times 10^6$ results are reported below.

Pressure distributions for the $Re_c = 1.6 \times 10^6$ condition at $\alpha = 0^\circ, 5^\circ, 8^\circ$ are shown in Fig. 10-12, respectively. The trailing edge pressure is estimated from a weighted average of the neighboring pressure ports. The CFD has good agreement with the experimental measurements.
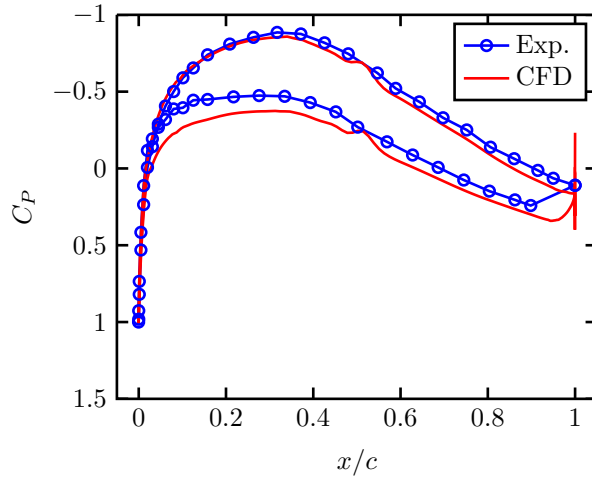
Figure 10: Pressure distribution for $Re_c = 1.6 \times 10^6$ at $\alpha = 0^\circ$, clean configuration.
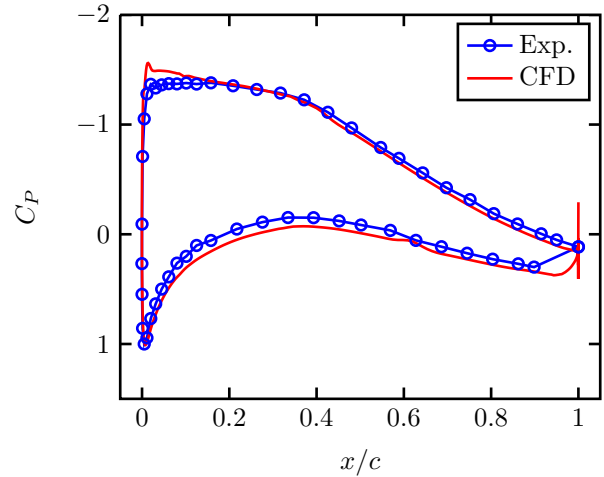
Figure 11: Pressure distribution for $Re_c = 1.6 \times 10^6$ at $\alpha = 5^\circ$, clean configuration.

The lift curve slope for the comparative cases is shown in Fig. 13. Within the linear region, the slope of both the experimental and CFD data match well to Abbott and von Doenhoff's data for a NACA 63_3-418.[33] As expected, the nonlinear region is less successful. CFD overpredicts stall, which is a common issue for computational methods. The experimental $c_{l,max}$ is slightly higher for $Re_c = 3.2 \times 10^6$. Both experimental
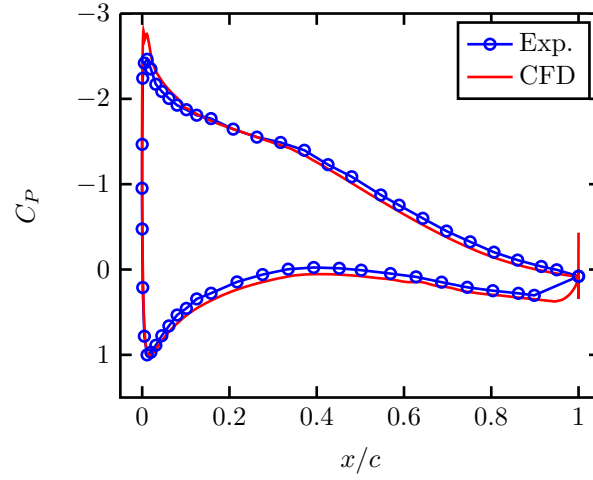
American Institute of Aeronautics and Astronautics

Figure 12: Pressure distribution for $Re_c = 1.6 \times 10^6$ at $\alpha = 8°$, clean configuration.

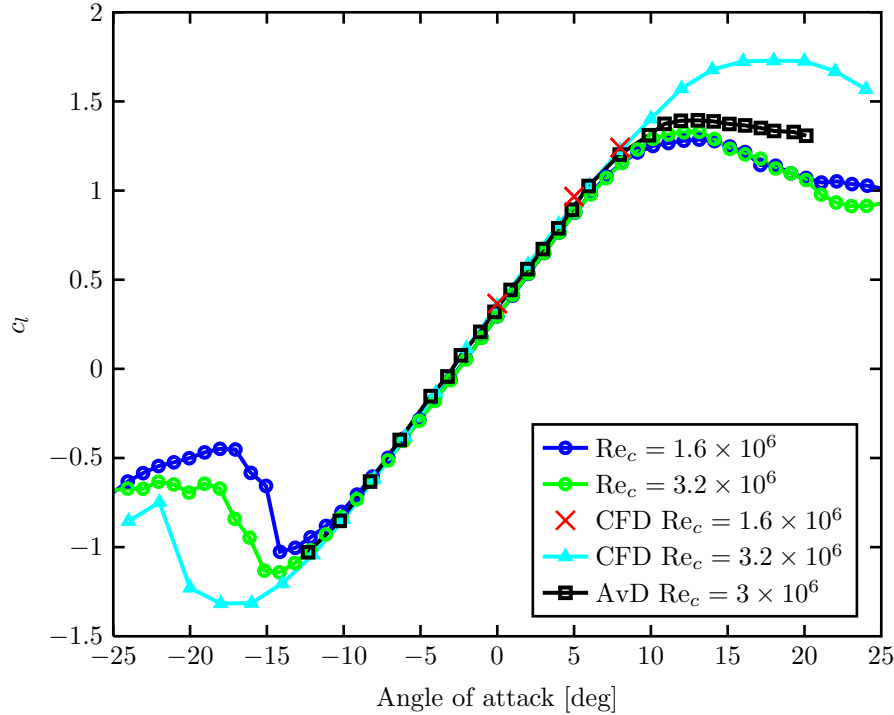curves diverge from Abbott and von Doenhoff after $\alpha = 9°$.

Figure 13: Lift curve slopes for the clean configuration.

Figure 15 illustrates the clean drag polars. The $c_{d,0}$ for the experimental polars is 6 counts higher compared to Abbott and von Doenhoff. Abbott and von Doenhoff tested in a low turbulence tunnel, with a $Tu \approx 0.05\%$, five times lower than the current investigation. The model in this test is modular, with small steps and gaps between the leading edge and main body interface. Therefore, matching drag data is not a primary goal in this investigation. Yet, in comparison to Abbott and von Doenhoff's original data, the drag for the clean configuration is deemed acceptable. The shape of the polars differs slightly at both smaller and larger lift coefficients. Particularly, for $Re_c = 1.6 \times 10^6$, the drag is high at negative lift and smaller at positive lift. For $Re_c = 3.2 \times 10^6$, the drag is low at negative lift and high and positive lift. The CFD matches well for $Re_c = 1.6 \times 10^6$. However, $Re_c = 3.2 \times 10^6$ overpredicts drag. The turbulence model

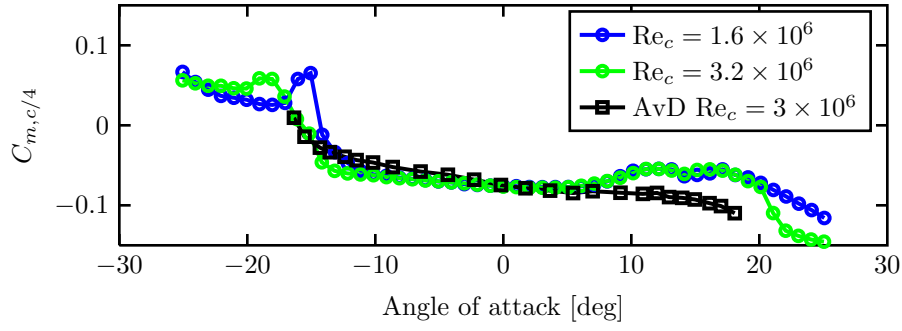American Institute of Aeronautics and Astronautics

Figure 14: Moment coefficient for the clean configuration.

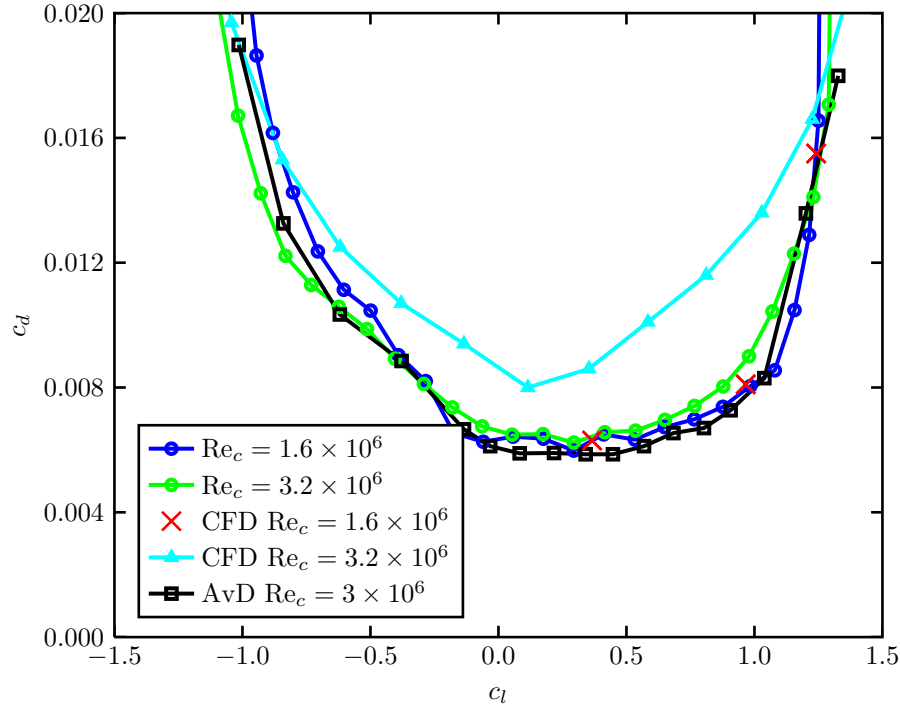transitions too early, causing a large drag rise.

Figure 15: Drag polars for the clean configuration.

An example of drag rise due to paint roughness is shown in Fig. 16. A consistent six count rise is seen in the paint roughness at $Re_c = 2.4 \times 10^6$. The drag rise is only noticeable between $-0.4 < c_l < 1.2$. Above or below this, it is equivalent to the clean configuration, suggesting an aft, 2D forward-facing step has a range of effectiveness to drag performance.

Transition locations are summarized in Fig. 17. The first black line represents a fit through $C_{P,\mathrm{min}}$, showing how the pressure minimum location evolves with angle of attack. The second black line is the transition point from XFOIL for an $N = 5$, while the next curve over represents $N = 9$. XFOIL utilizes an e^N lookup table for transition estimation and does not perform actual stability calculations. The blue and green lines represent data from IR images. The colored background (to be added) indicates transition for the $Re_c = 1.6 \times 10^6$ based on hotfilm data. Lastly, transition from CFD is shown with the red $\times$ symbol.

The IR and hoftilm data show excellent correlation to one another. An $N = 9$ fits well to the IR data. One drawback of IR data is that it fails to illustrate development of Tollmien-Schlichting (TS) waves. Using the comparison of IR and hotfilm, Fig. 17 illustrates that the IR data indicates when flow has become fully turbulent. The $Re_c = 3.2 \times 10^6$ case is also shown for comparison. The curve is similar to the $Re_c = 1.6 \times 10^6$
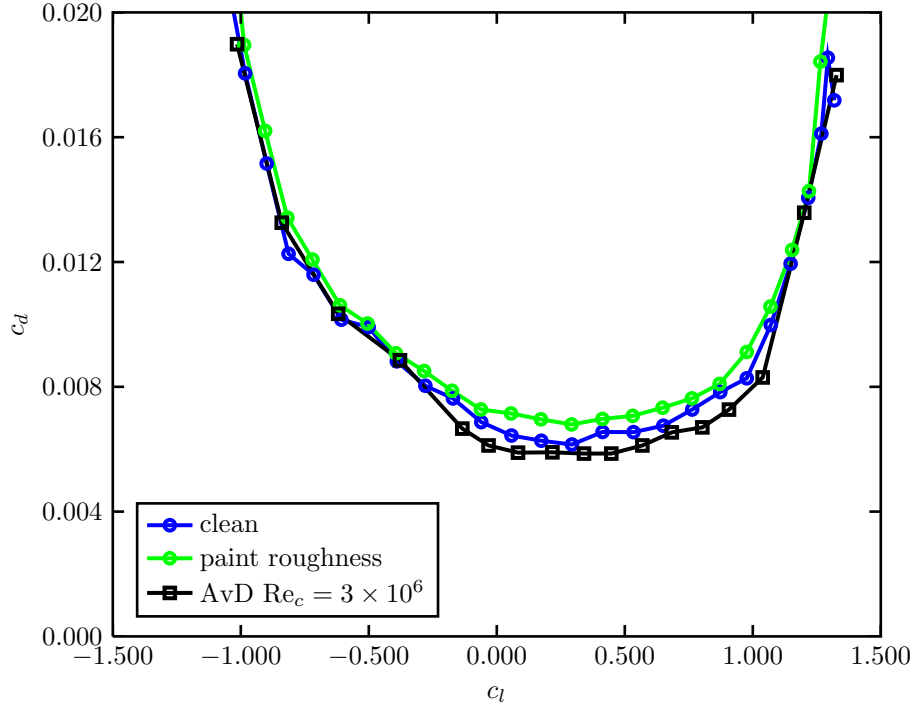
Figure 16: Drag polars for the paint configuration at $Re_c = 2.4 \times 10^6$.

with a constant shift, except for two additional inflection points. The transition model accurately predicts transition at $Re_c = 1.6 \times 10^6$.

The hotfilm spectra illustrate a fully laminar, transitional, and turbulent boundary layer in Figs. 18-20, respectively. Laminar flow is indicated by low baseline power spectra density (PSD) levels. Figure 19 shows a rise in PSD levels, particularly further aft on the model. Note that the 20% and 23% chord locations are still laminar. Also, a characteristic peak occurs around 1.5 kHz. The nondimensional frequency of a TS wave is $F = 2\pi f\nu/U_\infty^2$, which correlates to 130×10^{-6} for a dimensional frequency of 1.5 kHz, typical for an unstable TS wave. In Fig. 20, any indication of a TS wave is gone and the PSD are broadband noise.

Figure 21 represents boundary layer profiles at six different angles of attack. The profile is taken at 50% chord. The $y-$distance is measured from the airfoil wall normal. Angles of attack of $-4°$ and $0°$ indicate laminar flow. At higher angles, $8°$, $11°$, and $14°$, the boundary layer becomes progressively thicker and grows a larger deficit. At $\alpha = 16°$, the flow has separated, indicated by a large, nearwall region of nearly zero velocity.

Hotfilm CVA measurements yielding skin friction are shown in Figs. 22-25. The preliminary CVA measurements are compared to skin friction data from XFOIL assuming $N = 9$. The power spectra, shown and discussed above, indicate that each sensor on the hotfilm shown in Fig. 22 is laminar. The hotfilm data is consistently high, but follows the same trend. Figure 23 represents a transitional case with clear TS waves in the spectra. However, only the last sensor shows an increase in skin friction, suggesting that drag rises with a clear turbulent onset. Lastly, Fig. 25 represents a case where the spectra are clearly turbulent. Despite the well-defined spectra, the skin friction suggests a nearly transitioned turbulence flow. For comparison, Fig. 24 is included to show a more clear example of transition.

VIII.   Conclusion

A 2D, NACA 63_3-418 was tested at multiple Reynolds numbers and three configurations. One configuration represented realistic paint roughness designed from observations of in-service wind turbines. Numerous experimental measurements were obtained, including lift, drag, moment, boundary layer profiles, transition, and skin friction. Transition was acquired via IR thermography and hotfilm spectra. Results were compared to the Langtry-Menter CFD model at two Reynolds numbers. Lift for all cases matched well in the linear
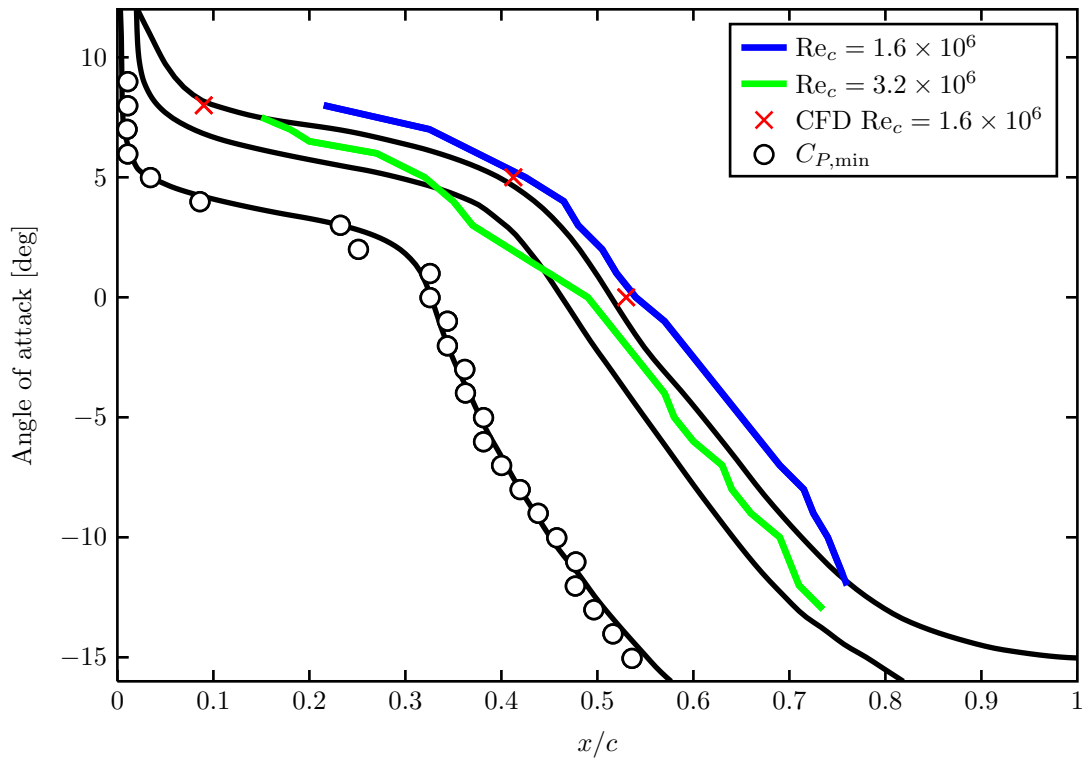
American Institute of Aeronautics and Astronautics

Figure 17: Freelogram for clean configuration.
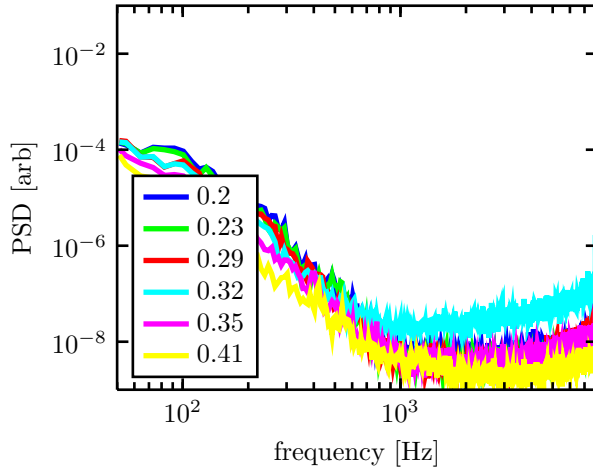

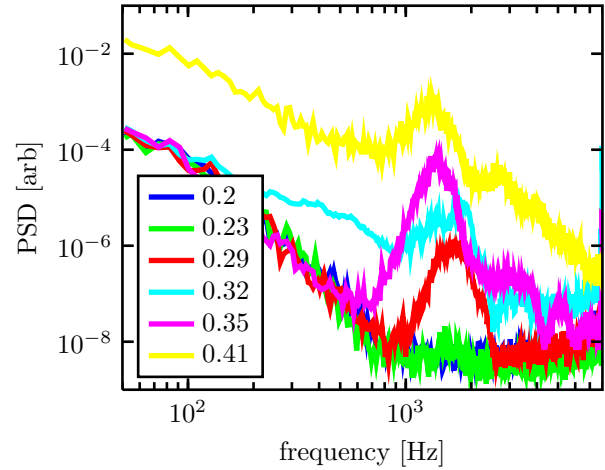Figure 18: Hotfilm spectra for clean configuration at $Re_c = 1.6 \times 10^6$ at $\alpha = 0°$.

Figure 19: Hotfilm spectra for clean configuration at $Re_c = 1.6 \times 10^6$ at $\alpha = 5°$.

region compared to historical data. Stall was poorly predicted, as expected. Simulations predicted drag at $Re_c = 1.6 \times 10^6$ well, but failed at $Re_c = 3.2 \times 10^6$, likely due to early transition. Differences between drag were observable between the clean and paint roughness configurations. Transition measurements compared well to one another, with the CFD also accurately predicting transition at $Re_c = 1.6 \times 10^6$. Skin friction data yielded additional information regarding transition location.
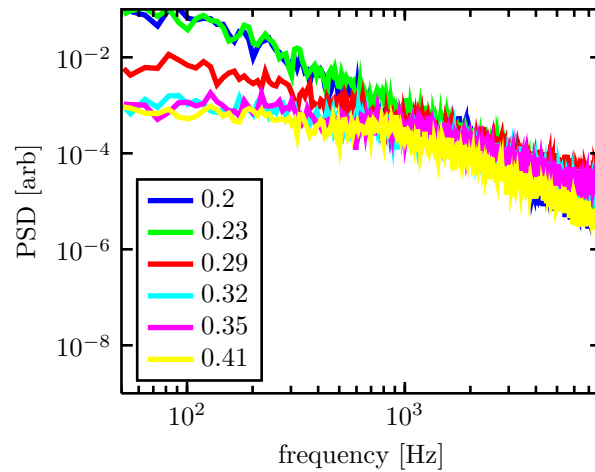
American Institute of Aeronautics and Astronautics

Figure 20: Hotfilm spectra for clean configuration at $Re_c = 1.6 \times 10^6$ at $\alpha = 8°$.

Acknowledgments

References

[1]Boccard, N., "Capacity factor of wind power realized values vs. estimates," *Journal of Energy Policy*, Vol. 37, 2009, pp. 2679.

[2]White, E. B., Kutz, D., Freels, J., Hidore, J. P., Grife, R., Sun, Y., and Chao, D., "Leading-Edge Roughness Effects on 63_3-418 Airfoil Performance," *49th AIAA Aerospace Sciences Meeting*, Vol. none, 2011, p. none.

[3]Berg, D. E., *A Review of the Workshop on WECS Blade-Surface Roughness*, Sandia National Laboratories, asme wind energy symposium ed., January 1994.

[4]Rempel, L., "Rotor Blade Leading Edge Erosion - Real Life Experiences," Wind Systems Magazine, Oct. 2012.

[5]of Energy, U. D., "20Contribution to U.S. Electicity Supply," DOE/GO-102008-2567, July 2008.

[6]Dryden, H. L., "Review of Published Data on the Effect of Rroughness on Transition from Laminar to Turbulent Flow," *Journal of the Aeronautical Sciences*, Vol. 20, 1953, pp. 477.

[7]Tani, I., "Boundary-Layer Transition," *Annual Review of Fluid Mechanics*, Vol. 1, 1969, pp. 169.

[8]Klebanoff, P., Schubauer, G. B., and Tidstrom, K., "Measurements of the Effect of Two-Dimensional and Three-Dimensional Roughness Elements on Boundary-Layer Transition," *Journal of the Aeronautical Sciences*, Vol. 22, 1955, pp. 803.

[9]Downs, R. S. I., White, E. B., and Denissen, N. A., "Transient Growth and Transition Induced by Random Distributed Roughness," *AIAA Journal*, Vol. 46, 2008, pp. 451.

[10]Ergin, F. G. and White, E. B., "Unsteady and Transitional Flows Behind Roughness Elements," *AIAA Journal*, Vol. 44, 2006, pp. 2504.

[11]Tangler, J. L. and Somers, D. M., "NREL Airfoil Families for HAWTs," *NREL/TP-442-7109*, 1995.

[12]Fuglsang, P. and Bak, C., "Development of the Risø Wind Turbine Airfoils," *Wind Energy*, Vol. 7, 2004, pp. 145.

[13]Bon, J. P., Taylor, R. P., McClain, S. T., and Rivir, R. B., "The Many faces of Turbine Surface Roughness," *Journal of Turbomachinery*, Vol. 123, 2001, pp. 739.

[14]Bons, J. P., "A Review of Surface Roughness Effects in Gas Turbines," *Journal of Turbomachinery*, Vol. 132(2), 2010.

[15]Reuss, R. L., Hoffman, M. J., and Gregorek, G. M., "Effects of Surface Roughness and Vortex Generators on the LS(1)-0417MOD Airfoil," Tech. Rep. NREAL/TP-442-6474, December 1995.

[16]Hidore, J. P., *Investigation of Data Quality for Wind Tunnel Internal Balance Testing*, Master's thesis, Texas A&M University, May 2013.

[17]Freels, J. R., *An Examination of Configurations for Using Infrared o Measure Boundary Layer Transition*, Master's thesis, Texas A&M University, 2012.

[18]Smith, A. M. O. and Clutter, D. W., "The Smallest Height of Roughness Capable of Affecting Boundary -Layer Transition," Douglas aircraft company, 1957.

[19]Barlow, J. B., Rae, W. H. J., and Pope, A., *Low-Speed Wind Tunnel Testing*, John Wiley & Sons, Inc., 3rd ed., 1999.
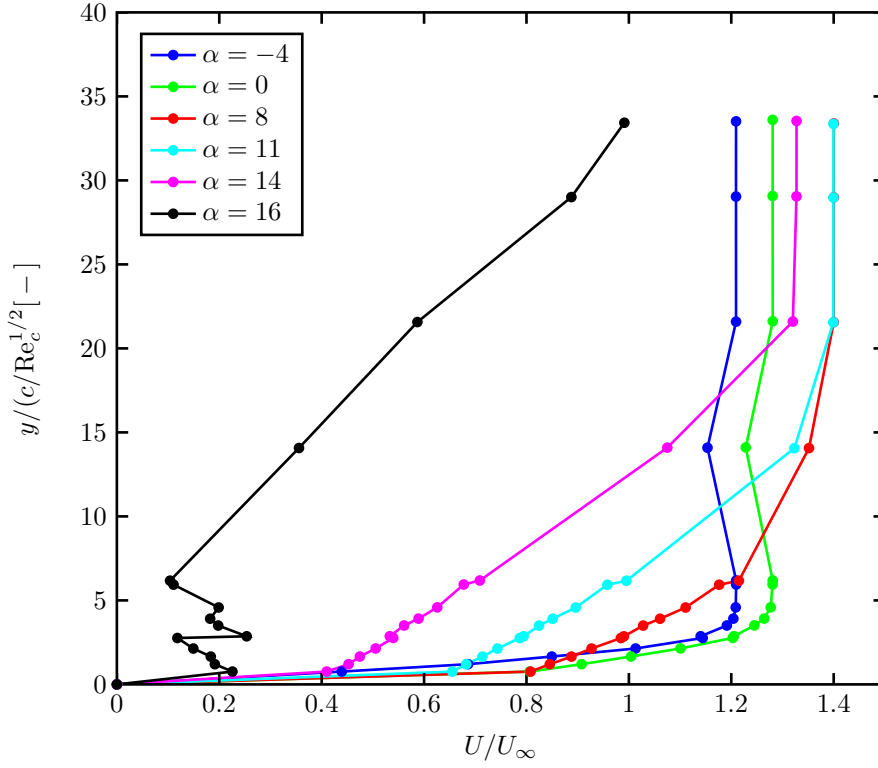
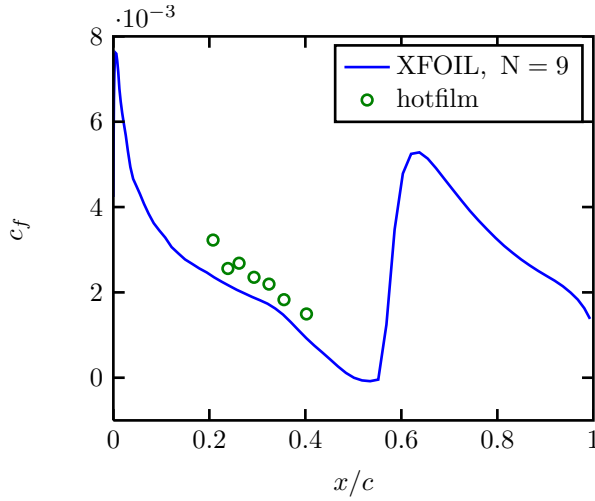Figure 21: Boundary layer profiles the for clean configuration at $Re_c = 1.6 \times 10^6$.

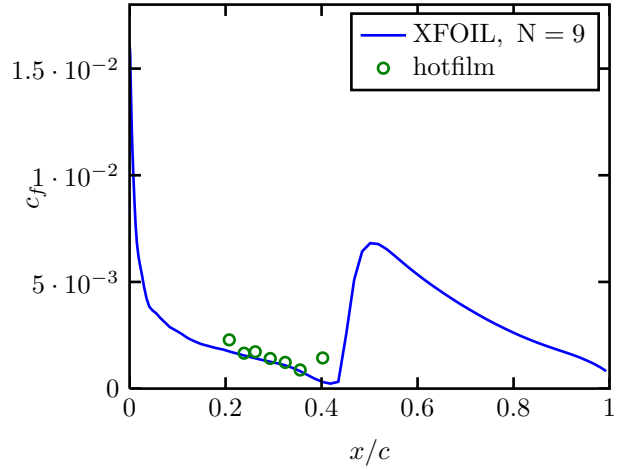Figure 22: Skin friction for clean configuration at $Re_c = 1.6 \times 10^6$ at $\alpha = 0°$.

Figure 23: Skin friction for clean configuration at $Re_c = 1.6 \times 10^6$ at $\alpha = 5°$.

[20]Sheldahl, R. E. and Klimas, P. C., "Aerodynamic Characteristics of Seven Symmetrical Airfoil Sections Through 180-Degree Angle of Attack for Use in Aerodynamic Analysis of Vertical Axis Wind Turbines," Tech. Rep. SAND80-2114, Sandia National Laboratories, 1981.

[21]Press, W. H., Teukolsky, S. A., Vetterling, W. T., and Flannery, B. P., *Numerical Recipes in C: The Art of Scientific Computing*, Cambridge University Press, New York, 2nd ed., 1992.

[22]van Ingen, J. L., "The e^N method for transition prediction. Historical review of work at TU Delft," *38th Fluid Dynamics Conference and Exhibit*, No. AIAA-2008-3830, Seattle, Washington, June 2008.
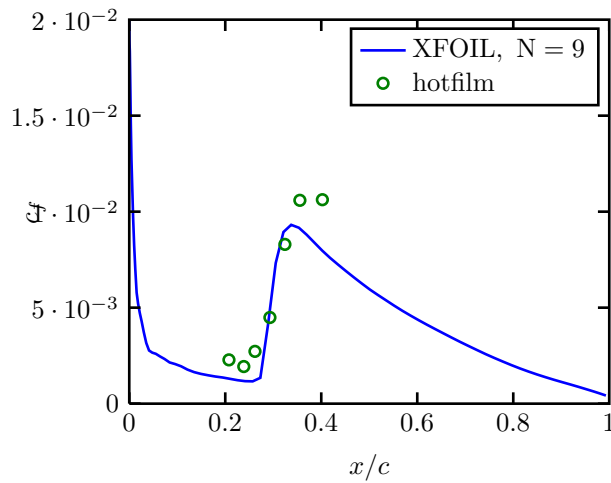
American Institute of Aeronautics and Astronautics

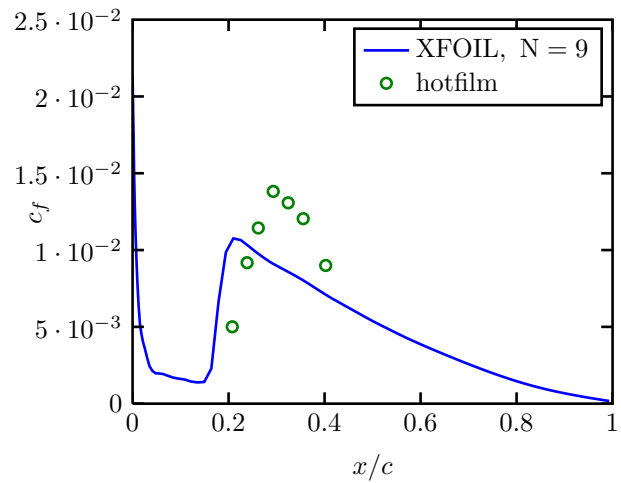Figure 24: Skin friction for clean configuration at $Re_c = 1.6 \times 10^6$ at $\alpha = 7°$.

Figure 25: Skin friction for clean configuration at $Re_c = 1.6 \times 10^6$ at $\alpha = 8°$.

[23]Menter, F. R., T., E., and Kubacki, S., "Transition Modeling Based on Local Variables," *Proceedings of the 5th International Symposium on Engineering Turbulence Modelling and Measurement*, edited by Elsevier, Amsterdam, 2002, pp. 555–564.

[24]Langtry, R. B., *A Correlation-Based Transition Model Using Local Variables for Unstructured Parallelized CFD Codes*, Ph.D. thesis, Univ. of Stuttgart, Stuttgart, Germany, 2006.

[25]Langtry, R. B. and Menter, F. R., "A Correlation-Based Transition Model for Unstructured Parallelized Computational Fluid Dynamics Codes," *AIAA Journal*, Vol. 47, No. 12, 2009, pp. 2894–2906.

[26]Dassler, P., Kozulovic, D., and Fiala, A., "Modeling of Roughness-Induced Transition Using Local Variables," *V European Conference on Computational Fluid Dynamics*, Lisbon, Portugal, June 2010.

[27]Abu-Ghannam, B. J. and Shaw, R., "Natural Transition of Boundary Layers: The Effects of Turbulence, Pressure Gradient, and Flow History," *Journal of Mechanical Engineering Science*, Vol. 22, No. 5, 1980, pp. 213–228.

[28]Jespersen, D. C., Pulliam, T. H., and Buning, P. G., "Recent Enhancements to OVERFLOW," *AIAA Paper 97-0644*, 1997.

[29]Beam, R. and Warming, R., "An Implicit Factored Scheme for the Compressible Navier-Stokes Equations," *AIAA Journal*, Vol. 16, No. 4, 1978, pp. 393–402.

[30]Feindt, E. G., "Untersuchungen ber die Abhngigkeit des Umschlages laminar- turbulent von der Oberflchenrauhigkeit und der Druckverteilung," *DFL Bericht*, Vol. 43, 1956.

[31]Kerho, M. F., *Effect of Large Distributed Roughness Near an Airfoil Leading Edge on Boundary-Layer Development and Transition*, Ph.D. thesis, Dept. of Aeronautical and Astronautical Engineering, Univ. of Illinois at Urbana-Champaign, Urbana, IL, 1995.

[32]Kerho, M. F. and Bragg M., B., "Airfoil Boundary-Layer Development and Transition with Large Leading-Edge Roughness," *AIAA Journal*, Vol. 35, No. 1, 1997, pp. 75–84.

[33]Abbott, I. H. and von Doenhoff, A. E., *Theory of Wing Sections*, Dover, 1959.

[34]Brodeur, R. R. and van Dam, C. P., "Transition Prediction for a Two-Dimensional Reynolds-averaged-Navier-Stokes Method Applied to Wind Turbine Airfoils," *Wind Energy*, Vol. 4, 2001, pp. 61–75.

[35]Dalili, N., Edrisy, A., and Carriveau, R., "A review of surface engineering issues critical to wind turbine performance," *Renewable and Sustainable Energy Reviews*, Vol. 13, 2009, pp. 428.

[36]Ferrer, E. and Munduate, "CFD Predictions of Transition and Distributed Roughness Over a Wind Turbine Airfoil," *47th AIAA Aerospace Sciences Meeting Including The New Horizons Forum and Aerospace Exposition*, No. AIAA-2009-0269, Orlando, Florida, 2009.

[37]Spruce, C. J., "Power performance of active stall wind turbines with blade contamination," *Proceedings of European Wind Energy Conference*, EWEC, Athens, 2006.

[38]Wilcox, D. C., *Turbulence Modeling for CFD*, DCW Industries, La Canada, California, 2nd ed., 1998.